Elevated Amyloidoses of Human IAPP and Amyloid Beta by Lipopolysaccharide and Their Mitigation by Carbon Quantum Dots

Journal:	*Nanoscale*
Manuscript ID	NR-ART-04-2020-002710.R1
Article Type:	Paper
Date Submitted by the Author:	10-May-2020
Complete List of Authors:	Koppel, Kairi; Monash University, ARC Centre of Excellence in Convergent Bio-Nano Science and Technology, Monash Institute of Pharmaceutical Sciences Tang, Huayuan; Clemson University, Physics and Astronomy Javed, Ibrahim; Monash Institute of Pharmaceutical Sciences, Drug Delivery, Disposition and Dynamics Parsa, Mehrdad ; Monash University, School of Chemistry Mortimer, Monika ; China Jiliang University, Institute of Environmental and Health Sciences, College of Quality and Safety Engineering Davis, Thomas; Monash University, Monash Institute of Pharmaceutical Sciences Lin, Sijie; Tongji University, Environmental Science and Engineering Chaffee, Alan; Monash University, School of Chemistry Ding, Feng; Clemson University, Physics and Astronomy Ke, Pu Chun; Monash University, ARC Centre of Excellence in Convergence Bio-Nano Science and Technology, Monash Institute of Pharmaceutical Sciences

Elevated Amyloidoses of Human IAPP and Amyloid Beta by Lipopolysaccharide and Their Mitigation by Carbon Quantum Dots

Kairi Koppel,[a] *Huayuan Tang,*[b] *Ibrahim Javed,*[c] *Mehrdad Parsa,*[d] *Monika Mortimer,*[e] *Thomas P. Davis,*[a,c*] *Sijie Lin,*[f] *Alan L. Chaffee,*[d] *Feng Ding*[b*] *and Pu Chun Ke*[g,a*]

[a] ARC Centre of Excellence in Convergent Bio-Nano Science and Technology, Monash Institute of Pharmaceutical Sciences, Monash University, 381 Royal Parade, Parkville, VIC 3052, Australia

[b] Department of Physics and Astronomy, Clemson University, Clemson, SC 29634, USA

[c] Australian Institute for Bioengineering and Nanotechnology, The University of Queensland, Brisbane Qld 4072, Australia

[d] School of Chemistry, Monash University, 17 Rainforest Walk, Clayton, VIC 3800, Australia

[e] Institute of Environmental and Health Sciences, College of Quality and Safety Engineering, China Jiliang University, Hangzhou, Zhejiang 310018, China

[f] College of Environmental Science and Engineering, State Key Laboratory of Pollution Control and Resource Reuse, Tongji University, 1239 Siping Road, Shanghai 200092, China

[g] Zhongshan Hospital, Fudan University, 111 Yixueyuan Rd, Xuhui District, Shanghai, 200032, China

Corresponding Authors

Email: Thomas Davis, t.davis@uq.edu.au; Feng Ding, fding@clemson.edu; Pu Chun Ke, pu-chun.ke@monash.edu.

KEYWORDS: lipopolysaccharide, IAPP, Aβ, amyloidosis, carbon quantum dot, zebrafish

Abstract

Type 2 diabetes (T2D) and Alzheimer's disease (AD) represent two most prevalent amyloid diseases with a significant global burden. Pathologically, T2D and AD are characterized by the presence of amyloid plaques consisting primarily of toxic human islet amyloid polypeptide (IAPP) and amyloid beta (Aβ). It has been recently revealed that the gut microbiome plays key functions in the pathological progression of neurological disorders through the production of bacterial endotoxins, such as lipopolysaccharide (LPS). In this study, we examined the catalytic effects of LPS on IAPP and Aβ amyloidoses, and further demonstrated their mitigation with zero-dimensional carbon quantum dots (CQDs). Whereas LPS displayed preferred binding with the N-terminus of IAPP and the central hydrophobic core and C-terminus of Aβ, CQDs exhibited propensities for the amyloidogenic and C-terminus regions of IAPP and the N-terminus of Aβ, accordingly. The inhibitory effect of CQDs was verified by an embryonic zebrafish model exposed to the peptides and LPS, where impaired embryonic hatching was rescued and production of reactive oxygen species in the organism was suppressed by the nanomaterial. This study revealed a robust synergy between LPS and amyloid peptides in toxicity induction, and implicated CQDs as a potential therapeutic against the pathologies of T2D and AD.

1. Introduction

Amyloid diseases are modern health epidemics impacting a significant portion of the global population. Type 2 diabetes (T2D), for example, is a most common metabolic disorder manifested by insulin deficiency and is pathologically manifested by the presence of extracellular amyloid plaques of human islet amyloid polypeptide (IAPP).[1] Alzheimer's disease (AD), on the other hand, is a primary form of neurological disorder characterized by impaired memory and cognition, and is pathologically indicated by the accumulation of extracellular plaques of amyloid beta (Aβ) and intracellular tau tangles. While Aβ interferes with neuronal communication at synapses, tau tangles block transport of nutrients and other molecules inside neurons.[2] The exact functional roles of IAPP and Aβ, however, remain unclear.[3,4]

Both IAPP and Aβ are inherently disordered peptides with a 25% overlap in sequence.[5] Specifically, IAPP is a 37-residue peptide co-synthesized, co-stored and co-secreted with insulin in pancreatic β-cell islets for glycemic control,[6,7] and is one of the most amyloidogenic peptides known. Aβ, in comparison, is produced by the cleavage of amyloid precursor protein (APP) and, despite its uncertain physiological functions, has been proposed to be involved in learning and brain development.[8,9] Aβ exists in various lengths, with the isomer $A\beta_{1\text{-}42}$ being the most hydrophobic and toxic.

Protein amyloid aggregation is a biophysical process whose endpoint is plaque formation. Many physiological and biological factors, such as secretase activities upon precursor protein cleavage, pH of the surrounding cellular environments, as well as ions, metals, ligands and chaperones, can affect the rate of fibrillization and fibrillar secondary structure.[10] Kinetically, amyloidosis exhibits a nucleation-dependent sigmoidal curve characterized by an initial nucleation phase, which is followed by an elongation phase and then a saturation phase.

Typically, disordered monomers first assemble into α-helical or β-sheet rich oligomers through primary and secondary nucleation, and the formed toxic oligomers then grow into protofibrils and eventually amyloid fibrils driven by hydrogen-bonding and hydrophobic interactions.[11,12]

In recent years, the roles of the gut microbiome in mediating amyloid diseases like T2D, AD, and Parkinson's disease (PD) have attracted much attention.[13–15] As part of the normal aging process, the gut microbiome decreases in diversity which affects the host's physiological function and overall wellbeing. Comparisons of the gut microbiome between healthy individuals and T2D, AD and PD patients have revealed that people carrying the diseases tend to have an imbalance towards certain bacterial taxa associated with pro-inflammatory reactions.[16,17] These bacterial taxa secrete metabolites and shed their cellular components, such as lipopolysaccharides (LPS), teichoic and lipoteichoic acids, which can enter systemic circulation via intestinal barriers with compromised integrity.[18,19] It has been shown that the metabolites produced by the gut microbiota are key factors underlying inflammation present in the brain.[20]

LPS is an outer membrane component of Gram-negative bacteria, an endotoxin which is a common pathogen-associated molecular pattern (PAMP) that is recognized by the innate immune system.[21,22] The cellular environment in the AD brain is characterized by over-activated microglial cells and inflammation that results in the inability of microglia to clear up amyloid plaques, which further triggers neuronal cell degeneration and memory loss.[23–26] Patients with the AD pathology tend to have elevated plasma concentration of LPS, and *post mortem* brain analysis has shown co-localization of LPS aggregates with amyloid plaques and within the neuronal nuclei of AD brains.[27,28] For example, when marmoset monkeys were injected with Aβ-LPS, not only it induced AD-like inflammation and co-localized with the amyloid peptide, but also accelerated the formation of plaques.[29]

Despite decades of research, no clinically viable solutions are available against amyloid diseases, as highlighted by repeated human trial failures employing peptidomimetics and antibodies. Owing to their unique physicochemical properties, nanomaterials have recently emerged as a viable therapeutic option, demonstrating potency against the amyloidoses of IAPP, Aβ and tau, among others.[30-36] Carbon quantum dots (CQDs), for example, are zero-dimensional, carbon-based nanostructures with an average size of 2-10 nm and an ability to cross the blood-brain barrier (BBB).[37] Since their discovery in 2004,[38] the biocompatible CQDs have generated much interest and increasing biomedical applications, including acting as an inhibitor against APP production and human insulin fibrillization.[37,39,40]

To understand the complex roles of bacterial endotoxins in the pathologies of amyloid diseases and to exploit the promise of nanomedicine, in the present study we examined the potential of CQDs in mitigating the aggregation and toxicity of IAPP and Aβ elevated by LPS. It should be pointed out that the role of LPS in IAPP amyloidosis has never been examined before, and the mode of association between LPS and Aβ remains unclear. Specifically, a thioflavin T (ThT) fluorescence assay, Fourier transform infrared (FTIR) spectroscopy and transmission electron microscopy (TEM) were used to assess changes in the fibrillization kinetics, peptide secondary structure and fibrillar morphology of IAPP and Aβ induced by LPS. The mitigating effect of CQDs on the impaired development of zebrafish (*Danio rerio*) embryos by the amyloid peptides and LPS was assessed. In addition, discrete molecular dynamics simulation revealed, for the first time, the molecular mechanisms of how LPS and CQDs bound to alternative sites on the peptides to impact their fibrillization. The potency of CQDs in counteracting the elevated amyloidoses of IAPP and Aβ by LPS, both *in vitro* and *in vivo*, implicated a therapeutic potential of the nanomaterial against human amyloid diseases.

2. Methods

Materials

IAPP (KCNTATCATQRLANFLVHSSNNFGAILSSTNVGSNTY; MW: 3905; purity: >95%) and Aβ (DAEFRHDSGYEVHHQKLVFFAEDVGSNKGAIIGLMVGGVVIA; MW: 4514; purity: >95%) were purchased from AnaSpec. The lyophilized powders were incubated with hexafluoro-2-propanol (HFIP) for 3 h, aliquoted and dried to ensure that the peptides were in their monomeric state before use. To prepare working solutions, the aliquots were dissolved in ~4 μL of 1% NH_4OH and further dissolved in MilliQ H_2O to a stock suspension at a concentration of 200 μM and used immediately. LPS from *Escherichia coli* O55:B5 was purchased from Merck and dissolved in MilliQ H_2O to achieve a 2 mg/mL stock.

Synthesis of carbon quantum dots (CQDs)

Uniform CQDs were produced using Victorian brown coal, from the Loy Yang mine (fixed carbon 47%, moisture 59%, ash 3.5% as received) as carbon precursor. A proprietary process was applied which started by the controlled oxidation of 50 g of brown coal in air. After cooling, 2 g of oxidized carbon was added to 100 mL distilled water and left to stand for 8 h (without stirring at ambient conditions) before being filtered through a filter paper (11 μm pore size, Whatman #1). The filtrate contained soluble CQDs. No further treatment or purification was applied.

Transmission electron microscopy (TEM)

TEM images were acquired using a Tecnai F20 electron microscope, operated at a voltage of 200 kV. Approximately 10 μL of a sample was transferred onto glow discharged formvar/carbon coated copper grids (400 mesh, Proscitech) and incubated for 60 s. Next, excess of the sample was removed by drawing liquid off with a filter paper, washed by dipping the grid into 5 μL of water, immediately air-dried and negatively stained with 5 μL of 1% uranyl acetate (UA) for 20 s. Excess UA was drawn off and the grids were air-dried before imaging.

Hydrodynamic diameter and zeta potential measurements

The hydrodynamic diameter and zeta potential of CQDs were determined using a Malvern Zetasizer Nano-ZS and analyzed by Zetasizer Software 7.02. The samples (0.5 mg/mL) were suspended in MilliQ H_2O and measured at room temperature in triplicate.

Fourier transform infrared (FTIR) and Raman spectroscopy

FTIR absorption spectra of CQDs were collected using Bruker Equinox, IFS-55, running 64 scans at resolution of 4 cm^{-1}. Samples were prepared as KBr disks after vigorously mixing 2 mg of degassed CQDs with 200 mg of dried KBr. For the peptide FTIR spectra, samples were incubated at 37 ºC for 15 h and 30 h for IAPP and Aβ, respectively, in consideration of their different amyloidogenic efficacies. At 0 h and 15/30 h, 100 μL of each sample was freeze-dried. For measurement, the lyophilized peptide powder was either directly placed on a sample holder or dissolved in 5-10 μL of MilliQ H_2O and air-dried on a sample holder. FTIR spectra were acquired between 1,560-1,740 cm^{-1} (resolution: 4 cm^{-1}) at 20 °C. Blank spectra were automatically subtracted from the spectra of the samples. Peak fitting and data analysis were performed using Origin software with built-in application PeakDeconvolution (OriginLab). Raman spectra were collected on a Renishaw inVia Raman microscope (Olympus, 50× long working-distance lens) with excitation at 488 nm and 1 mW power, using a 20 s rate extended mode scan and then baseline corrected.

X-ray photoelectron spectroscopy (XPS)

XPS was performed using an AXIS Ultra DLD spectrometer (Kratos Analytical, Manchester, UK) with a monochromated Al K_α source at a power of 180 W (15 kV · 12 mA), a hemispherical analyzer operating in the fixed analyzer transmission mode and the standard aperture (analysis area: 0.3 mm × 0.7 mm). The total pressure in the main vacuum chamber during analysis was typically between 10^{-9} and 10^{-8} mbar. Survey spectra were acquired at a pass energy of 160 eV. To obtain detailed information about the chemical structure and oxidation states of the CQDs, high-resolution spectra were recorded from individual peaks at 40 eV pass energy. Peak positions on the binding energy scale were corrected by setting the graphitic carbon peak to 284.5 eV. The samples were filled into shallow wells of a custom-built sample holder and analyzed at a nominal photoelectron emission angle of 0º with respect to the surface normal. Since the actual emission angle is ill-defined for nanoparticles (ranging from 0º to 90º), the sampling depth ranged from 0~10 nm. Data processing was performed using CasaXPS processing software, version 2.3.15 (Casa Software, Teignmouth, UK). All elements present were identified from the survey spectra. The atomic concentrations of the detected elements were calculated using integral peak intensities and the sensitivity factors were supplied by the manufacturer.

Thioflavin T (ThT) kinetic assay

To assess the fibrillization kinetics of IAPP and Aβ in the presence of LPS and CQDs, a freshly prepared 600 μM ThT solution was mixed with samples at a 1:2 molar ratio of ThT/peptide. The assays were performed at 37 ºC on a black, clear bottom 96-well plate (Costar) and changes in ThT fluorescence were recorded every 10 min over 15-25 h, at excitation/emission 440/484 nm using a microplate reader (PerkinElmer, EnSpire 2300). All samples were analyzed in triplicate.

Zebrafish hatching assay and reactive oxygen species (ROS) measurement

A hatching assay using zebrafish (*Danio rerio*) embryos was performed as described previously.[41] The wild-type zebrafish was maintained in a 14/10 h light/dark cycle in the fish water circulatory system. Embryos were produced by adult spawning, with the first light in the morning, and were then washed with methylene blue and Holtfreter's buffer. Healthy embryos at 3 h post fertilization (hfp) were selected for microinjection. Different samples, i.e., LPS (1 and 10 μM), CQDs (0.5 μg/mL), and LPS (1 μM) with and without CQDs (0.5 μg/mL), IAPP (10 μM) or Aβ (10 μM) were microinjected to the embryos. H_2O_2 (10%) and Holtfreter's buffer were used as positive and negative controls, respectively. The samples with IAPP or Aβ also contained 20 μM of the ThT dye. Each sample was tested in triplicate, with each consisting of 10 embryos. Microinjections were performed with a 10 nL injection volume and 20 psi injection pressure (PV830 Pneumatic Picopump, WPI). After microinjection, the embryos were incubated at 28 + 0.5 °C in a 96-well microplate containing 200 μL Holtfreter's buffer per well. The embryos were imaged at 3 h post injection using the green and bright-field channels of a fluorescence microscope (EVOS FL Auto, Life Technologies). The hatching rate of the embryos was determined at 3 days post injection. Generation of ROS was measured after microinjecting the embryos with the same samples as above, but without ThT dye. The sample was mixed with 2',7'-dichlorodihydrofluorescein diacetate (H_2DCFDA) prior to microinjection. The embryos were incubated for 12 h after injection, homogenized in Holtfreter's buffer in a Teflon glass homogenizer (70 Hz for 1 min) and DCF fluorescence was quantified in a microplate reader with excitation/emission at 495/529 nm. H_2O_2 (10%) and Holtfreter's buffer were used as positive and negative controls, respectively, for the ROS assay. All zebrafish experiments were performed in accordance with the ethical guidelines of Tongji University and the experiment protocols were approved by the Animal Center of Tongji University (Protocol #TJLAC-019-113).

Molecular dynamics simulations

Computer simulations were performed with the all-atom discrete molecular dynamics (DMD).[42] Replacing the classic continuous interaction potentials with discrete stepwise functions,[43] DMD simulations allow increased sampling efficiency and have been used by our group and others to study protein folding, amyloid aggregation, and interactions with nanoparticles.[32,34-36,44-46] Interatomic interactions including van der Waals (VDW), solvation, hydrogen bonds and electrostatic interactions in our all-atom DMD simulations were adapted from the Medusa force field,[47] which was benchmarked for accurate prediction of protein stability change upon mutation[48] and protein-ligand binding affinity.[49] The force field parameters for VDW, covalent bonds, bond angles and dihedrals were taken from CHARMM19.[50] An implicit solvent model, named effective energy function proposed by Lazaridis and Karplus,[51] was used in the simulations. The formation of hydrogen bonds was modelled by a reaction-like algorithm.[52] The screened electrostatic interactions were computed using the Debye–Huckel approximation with the Debye length set to 10 Å, corresponding to a monovalent salt concentration of 100 mM.

The molecular structure of LPS used in the simulations was obtained from PubChem (CID: 46173313) and the initial structures of IAPP and Aβ were taken from protein databank (PDB ID: 2L86 and 1z0q, respectively).[53] A CQD of 3 nm in diameter, consisting of 1679 atoms, was constructed using Avogadro[54] and the surface was randomly decorated with oxygen-containing functional groups including 55 hydroxyls and 21 carboxyls. The initial CQD structure was relaxed with a 100-ns simulation. To mimic the relatively low experimental concentrations of LPS and CQDs with respect to the peptides, the aggregation simulation systems were comprised of four peptides, one LPS and/or one CQD if applicable. A cubic simulation box with a periodic boundary condition and a dimension of 11.1 nm was used. For each molecular system, 20 independent simulations with different initial configurations and velocities were performed. The temperature was maintained around 300 K using the Anderson's thermostat. The time step in simulations was 50 fs and the structures were saved every 100-time steps for analysis. Each independent simulation lasted 500 ns for the systems with IAPP peptides and 700 ns for the systems with Aβ peptides. The last 100-ns simulations after reaching steady states were used for analyses. An inter-atomic distance cut-off of 0.55 nm was adopted for defining an atomic contact in data analysis, and the DSSP algorithm[55] was used to define the secondary structures.

3. Results and discussion

Characterizations of CQDs

TEM imaging showed highly monodisperse CQDs with an average diameter of 2.8 nm (**Fig. 1A**). The dynamic light scattering (DLS) measurement of the CQDs yielded a broad peak at 10-80 nm with a maximum at ~25 nm. The FTIR spectra of the CQDs revealed existence of significant amounts of oxygen and nitrogen functional groups, including carboxylic (HO-C=O)/carboxylate (O-C=O) stretching at 1700 cm^{-1}/1425 cm^{-1}, ether/phenolic deformation at 1180-1235 cm^{-1}, C-O/C-N stretching at 1050 cm^{-1}, and O-H/N-H stretching at 3360 cm^{-1} and bending at 1350 cm^{-1} (**Fig. 1B**).[56–58] The existence of significant amounts of carboxyl groups, located at the edges of CQDs, resulted in negative charges due to the ionization of the carboxylic groups, as confirmed by the zeta potential of -44.6±7.9 mV for the nanoparticles. This property entailed excellent water dispersity of the CQDs free from turbidity, at concentrations as high as 11 mg/mL, even after one-year storage at ambient lab conditions.

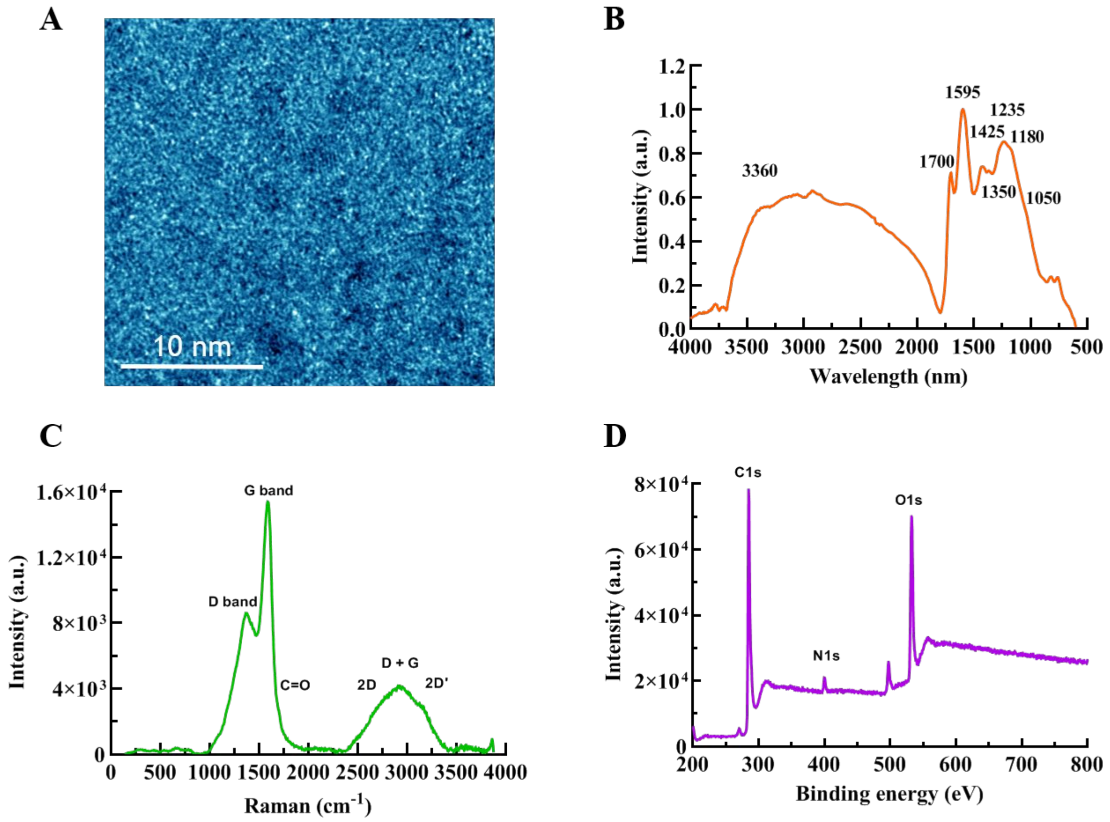

Figure 1. Characterizations of CQDs. TEM image (**A**), FTIR (**B**), Raman (**C**) and XPS survey spectra (**D**) of CQDs.

The Raman spectrum showed a D band (attributed to sp^3-hybridized amorphous carbon atoms) at 1370 cm^{-1} and a G band at 1586 cm^{-1} (attributed to sp^2-hybridized graphitic carbon atoms),[59–61] as well as a peak at 1702 cm^{-1} that is characteristic of carbonyl groups (**Fig. 1C**).[62] In addition, a broad peak in the second-order region of the spectrum was observed that, it appears, might be de-convolutable into three peaks at 2690 cm^{-1} (G′), 2930 cm^{-1} (D + G band) and 3160 cm^{-1} (2D′), respectively.[60] The ratio of the peak intensities, $I_D/I_G = 0.56$, indicated a high proportion of graphitic carbon structures and was higher than the values reported for most CQDs synthesized from other natural carbon sources.[61,63–65]

The curve-fitted C1s XPS spectrum of the CQD’s (**Figs. 1D&S1**) indicated occurrence of two types of non-oxygenated carbon. Specifically, the spectrum indicated sp^2 C-C bonds of graphitic structures at 284.5 eV and sp^3 non-graphitic C–C bonds forming the main feature at 285.0 eV. In addition, the presence of four different carbon-heteroatom functional groups was inferred: C-N (at 285.7 eV), C-O-C/C-O-H (at 286.7 eV), C=O/C-N (at 288.1 eV), and HCO_2 (at 288.8 eV).[58,66] The curve-fitting of the nitrogen high-resolution region revealed three peaks: 399.1 eV for tertiary N/aromatic amine, 400.6 eV for pyrrolic nitrogen and 402.5 eV for quaternary nitrogen.[66,67] The determined XPS surface atomic percentage of carbon, oxygen and nitrogen was 75%, 19.5% and 2.8%, respectively.

Aggregation of IAPP and Aβ and their modulation by LPS and CQDs

The interaction between $A\beta_{25\text{-}35}$ and LPS was first studied by Asti and Gioglio using TEM. Upon 2 weeks of incubation, $A\beta_{25\text{-}35}$ fibrils appeared to be in close contact with LPS and possible potentiation of $A\beta_{25\text{-}35}$ occurred.[68] In comparison, the effect of LPS on IAPP amyloidosis remains entirely unknown. Similar to AD subjects, T2D patients experience altered gut microbiome towards Gram-negative bacteria and are further subject to chronic infections due to implications from the disease.[69] This can lead to elevated LPS levels to cause pancreatic injury,[70] which may create opportunities for the endotoxin to interact with IAPP, among others.

Structurally, LPS consists of a hydrophobic lipid A and a hydrophilic core of polysaccharide, and is aggregation prone in aqueous solutions.[71,72] The LPS aggregates resemble cell membranes (**Fig. S2A**) and may therefore act as a nucleation center for peptide fibrillization.[73-75] To evaluate the effect of LPS on amyloidosis, we prepared LPS of 20 μg/mL (around its critical micelle concentration[76]), which was further diluted for experiments. Both the amyloid aggregation kinetics of IAPP and Aβ followed standard Sigmoidal curves, with IAPP fibrillization reaching plateau in 6 h and Aβ aggregation not reaching the maximum by 20 h (**Fig. 2A&2B**, red curves). The lag time of Aβ fibrillization was shortened by 4 h in the presence of LPS, while the effect of LPS on IAPP fibrillization appeared to be less pronounced (**Fig. 2B; controls in Fig. S3**). The smaller reduction in the lag time of IAPP fibrillization was likely due to the already rapid aggregation of the peptide itself, i.e., over 6 h compared to 20 h for Aβ (**Fig. 2A&B**). For TEM imaging, the IAPP and Aβ samples were incubated for 15 h and 30 h, respectively, to ensure the presence of mature fibrils in the control samples (**Fig. 2C&G**). In the presence of LPS, the amount of fibrils was similar to the control, i.e., peptides without LPS, although the fibrils were more intertwined, suggesting the effect of LPS on concentrating the peptide oligomers to lower the nucleation energy barrier in aggregation **(Fig. 2D&H, Fig. S2B)**.[77]

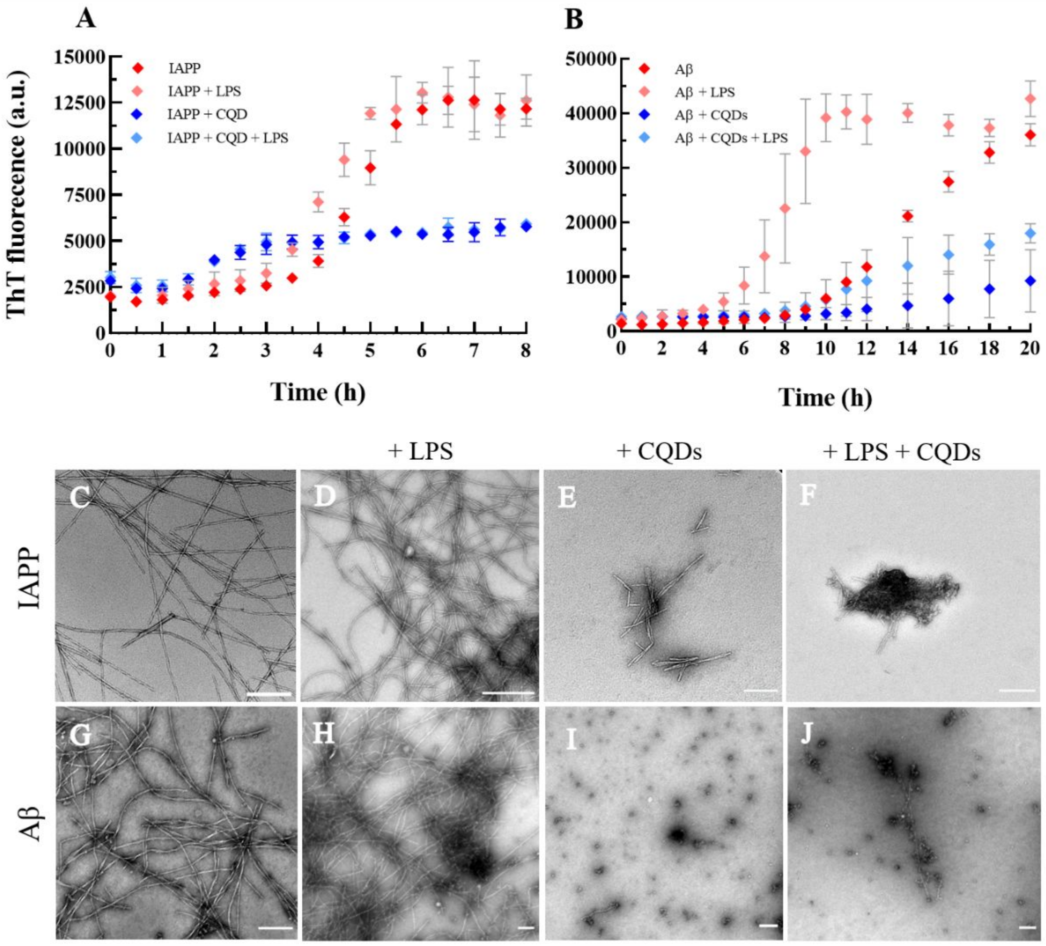

Figure 2. Aggregation kinetics and morphologies of IAPP and Aβ in the presence of LPS and CQDs. 25 μM IAPP and 50 μM Aβ were incubated with LPS (0.78 μg/mL) and CQDs at

a molar ratio of 1:2 and 1:1, respectively (peptide/CQDs). The ThT assay results (**A** for IAPP, **B** for Aβ) demonstrate a greater enhancement of Aβ amyloidosis by LPS than for IAPP, whereas CQDs effectively mitigated the fibrillization in both cases. TEM imaging of IAPP (**C-F**) and Aβ (**G-J**) revealed more intertwined fibrils upon co-incubating the peptides with LPS compared to all other cases. Scale bars: 200 nm.

The molar ratio of peptide/CQDs was set at 1:2 and 1:1 for IAPP and Aβ, respectively. CQDs were able to inhibit IAPP fibrillization effectively, resulting in only small oligomers and aggregates devoid of long fibrils. Due to the good suspendability of the CQDs, we did not observe notable concentration dependence for CQDs to effectively interact with IAPP/Aβ and LPS. The resulting aggregates appeared morphologically different for IAPP and Aβ (**Fig. 2E&F, I&J**). This may be due to the different binding mechanisms between CQDs and the two peptides in mitigating the amyloidoses, as revealed in detail by DMD simulations summarized below.

Structural changes of IAPP and Aβ induced by LPS and CQDs

FTIR was used to assess changes in mature peptide fibrils induced by LPS and CQDs (**Fig. 3A&B**). As monomers self-assemble into fibrils, their secondary structure evolves from unstructured, α-helix rich monomers and oligomers to β-sheet rich fibrils.[5,78] For sample preparation, IAPP, Aβ, LPS and CQD concentration and incubation conditions were kept the same as for the ThT assay and TEM imaging. At a chosen time point, samples were freeze-dried and IR spectra were obtained. After obtaining initial spectra between 1560-1740 cm^{-1}, the data was de-convoluted using Origin software Peakfit app. The IR peaks were assigned to secondary structures following the literature (**Table S1**).[79]

After 15 h of IAPP fibrillization, more than half of their α-helices were converted into β-sheets. LPS did not induce much difference in the peptide secondary structure (**Fig. 3A**), suggesting that LPS acted as a nucleation center for catalyzing IAPP fibrillization. The ThT fluorescence intensity, reflective of the peptide β-sheet content, was also similar in mature fibrils with and without LPS, further supporting the FTIR data (**Figs. 2A&3A)**. Similar FTIR results were obtained for Aβ, where the secondary structure in the presence of LPS was similar to the control (**Fig. 3B**). The resulting aggregates differed in the morphologies of IAPP and Aβ in the presence of CQDs (**Fig. 2E&I**), where more extensive reduction in the β-sheet content occurred for IAPP than for Aβ (**Fig. 3A&B**), indicating that CQDs inhibited IAPP amyloidosis more effectively. In the presence of both LPS and CQDs, most of the resulting aggregates in the case of Aβ still carried a relatively high β-sheet content (**Fig. 3B**) but assumed the conformation of non-toxic, amorphous aggregates (**Fig. 2J**).

We used DMD simulations to investigate the effects of LPS and/or CQD on the aggregation of IAPP and Aβ. In the presence of LPS, the size of IAPP oligomers increased more rapidly and formed larger aggregates in equilibrium compared to the control of IAPP alone (**Fig. S4A**). The β-sheet contents of IAPP were also promoted by LPS (**Fig. S4B**). The acceleration of IAPP oligomerization and promotion of β-sheet formation by LPS *in silico* is consistent with the experimental observation that LPS reduced the lag-time of IAPP aggregation (**Fig. 2A**). In contrast, the presence of CQD inhibited the formation of β-sheet structures of both IAPP and Aβ with and without LPS (**Fig. S4B&F**), in agreement with the ThT assay and TEM observations (**Fig. 2**). Consistent with the FTIR results, DMD simulations also predicted noticeable variations of the overall peptide secondary structure contents induced by CQD, whereas the effects of LPS were insignificant (**Fig. S5A&F)**.

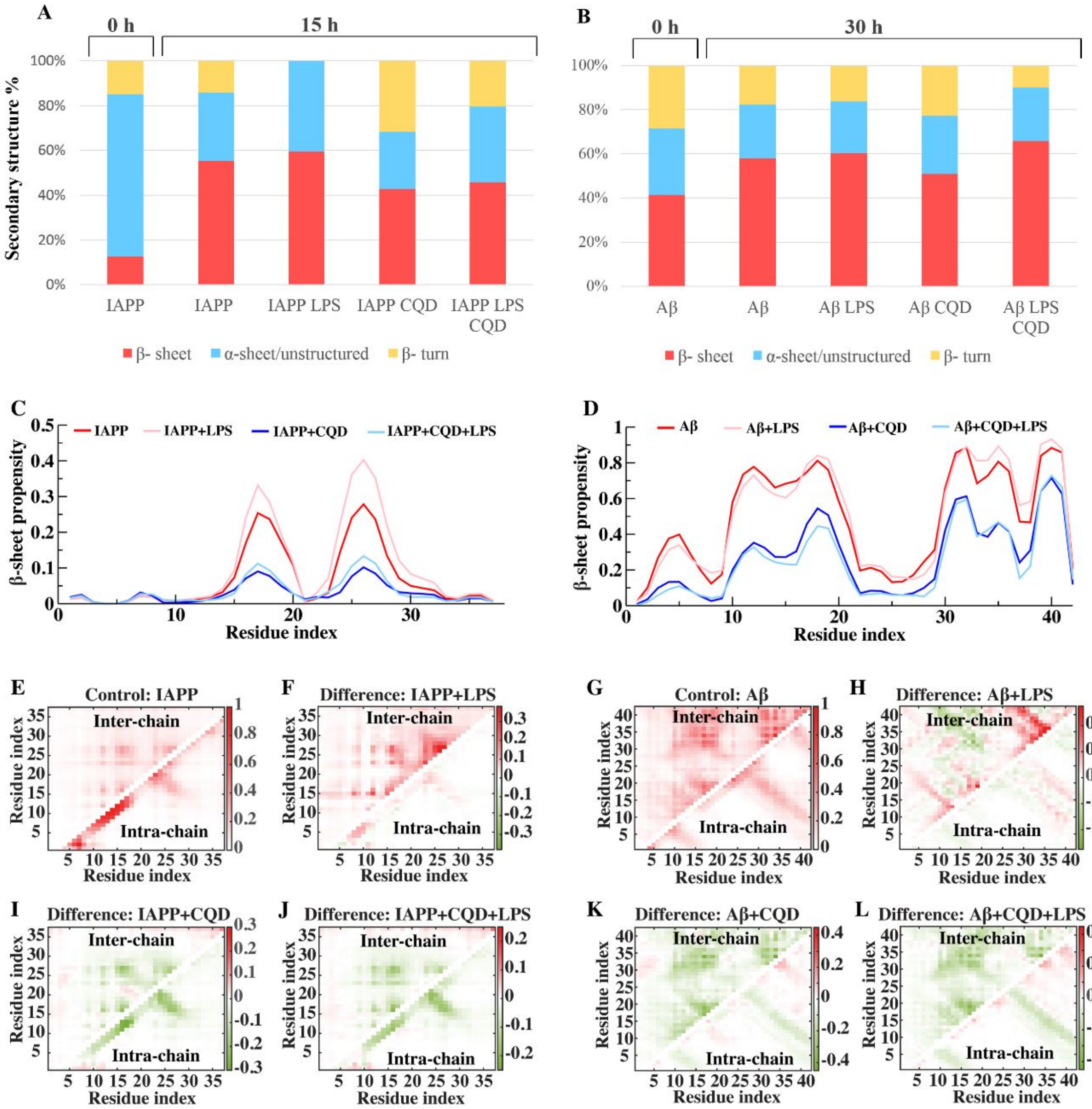

Figure 3. Characterization of the secondary structures of IAPP and Aβ in the presence of LPS and CQDs. Relative abundance of secondary structures of IAPP (**A**) and Aβ (**B**) as measured by FTIR. IAPP and Aβ were incubated at 37 ºC, at 25 µM and 50 µM and for 15 h and 30 h, respectively. The β-sheet propensity of each residue in IAPP (**C**) and Aβ (**D**) was derived from DMD simulations with the peptides alone and in the presence of LPS, CQD, or both (CQD+LPS). Compared to the inter- (upper diagonal) and intra-chain (lower diagonal) contact frequency maps of IAPP (**E**) and Aβ (**G**) aggregation alone, the changes of contact frequency maps are shown in the presence of LPS (IAPP in **F**, Aβ in **H**), CQD (IAPP in **I**, Aβ in **K**), and both (IAPP in **J**, Aβ in **L**).

Interestingly, the effects of LPS on the oligomerization dynamics of Aβ were subtle in terms of the time evolution of oligomer sizes and the overall β-sheet content in the simulations (**Fig. S4E, F**). To understand this apparent inconsistency with the ThT data for Aβ+LPS (**Fig. 2B**) and gain more insight into the interactions of peptides in the presence of LPS and/or CQDs, the secondary structure propensity of each residue (**Fig. 3C&D**, **Fig. S6**) and the residue-wise inter- and intra-chain contact frequency maps (**Fig. 3E-L**) were calculated after the simulations reached steady states. For IAPP, the presence of LPS increased the overall inter-chain contacts (**Fig. S4C**) with a noticeable enhancement of inter-peptide contacts between the amyloidogenic region of IAPP (residues 22-29) (**Fig. 3F**). As a result, the β-sheet propensity of IAPP residues, especially in the amyloidogenic region, was promoted (**Fig. 3C, Fig. S6A-C**). For Aβ aggregation in the presence of LPS, the β-sheet propensities of residues 16-21 and 31-40 (near the two known amyloidogenic regions of Aβ16-22 and 25-35) were slightly increased compared to the control, although the overall β-sheets remained the same due to decreased β-sheet content in other regions, likely due to electrostatic repulsion between the negatively charged Aβ (D1,E3,D7,E11,E22,D23) and LPS (**Fig. 3D, Fig. S5F and Fig. S6D-F**). Despite a lack of major changes in the total number of inter-chain contacts (**Fig. S4G**), the presence of LPS increased interactions along the diagonal region and reduced the interactions off-diagonal of the inter-chain contact frequency map (**Fig. 3H**) compared to the control (**Fig. 3G**), indicating the promotion of in-registered parallel alignments of peptides in the oligomers. Since all the solved fibril structures of Aβ and other proteins/peptides in the literature featured in-registered parallel β-sheets (e.g., **Fig. S7**), nucleation of in-registered parallel β-sheets of the oligomers is likely the rate-limiting step of amyloidosis. Hence, our simulations revealed that LPS accelerated Aβ fibrillization by promoting the formation of in-registered parallel alignment of peptides in the oligomers, subsequently reducing the free-energy barrier of nucleation. Besides, all the Aβ peptides fully aggregated into a large oligomer (**Fig. S4E**) with high β-sheet contents (**Fig. S4F**) in a short time due to the high concentration in simulations, whereas the LPS concentrated the Aβ with initially low concentration to nucleate the fibrillization in ThT kinetic assay as revealed by the TEM imaging (**Fig. 2G&H**). Thus, the promotion effect of LPS on the oligomerization dynamics of Aβ was hidden in simulations. The enhancement of inter-chain contact frequency maps along the diagonal was also observed for IAPP aggregation in the presence of LPS (**Fig. 3F**). In contrast, CQD reduced both intra- and inter-chain contacts of IAPP and Aβ with and without LPS (**Fig. 3I-L**, **Fig. S4C&D, G-H**), resulting in a reduction of the β-sheet content and promotion of coils and bends (**Fig. 3C&D, Fig. S6**).

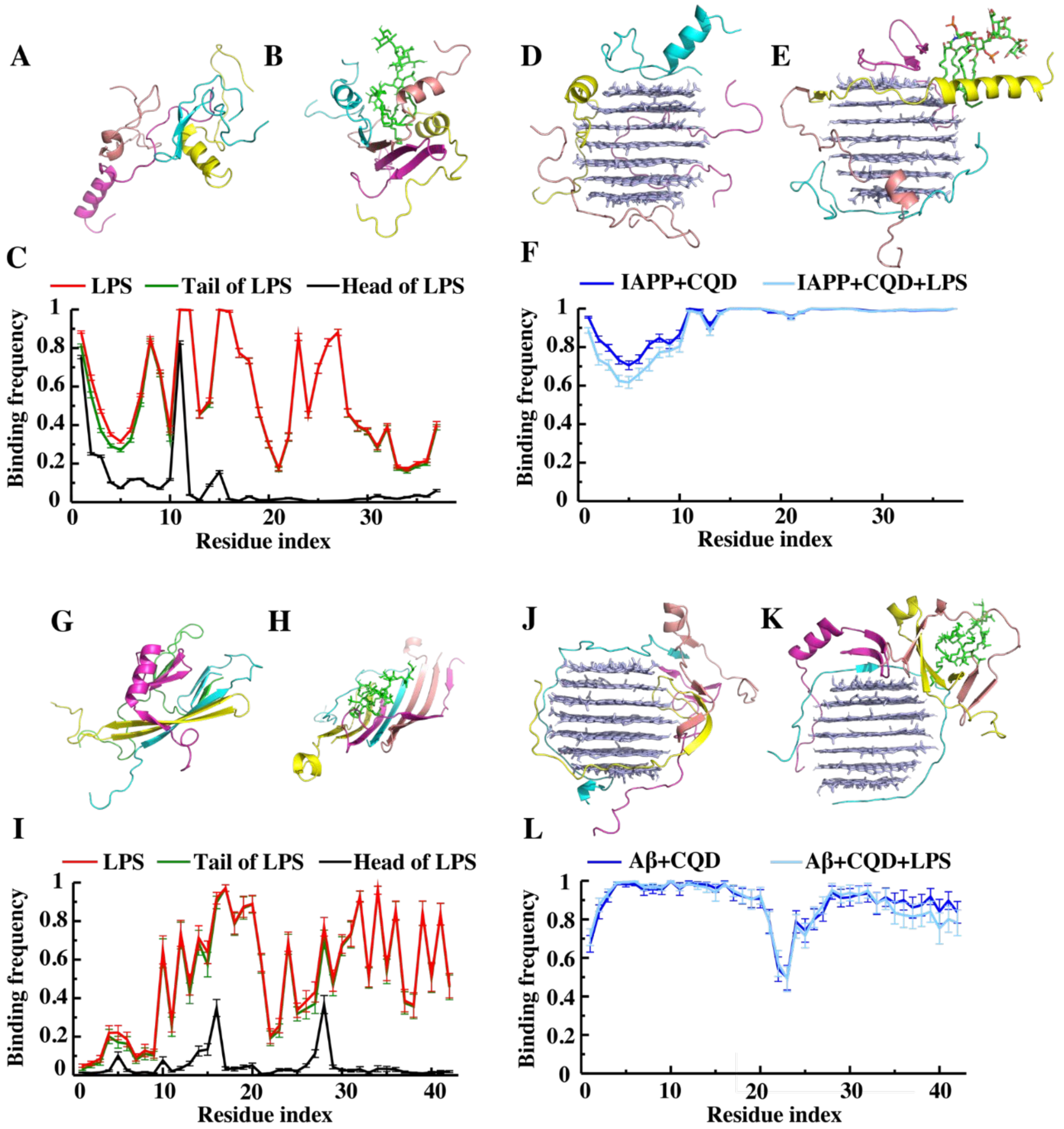

Figure 4. Interactions of LPS and CQD with IAPP and Aβ in DMD simulations. Snapshot structures of IAPP (**A**), IAPP+LPS (**B**), IAPP+CQD (**D**) and IAPP+CQD+LPS (**E**). Binding frequency of each IAPP residue with LPS (**C**) and CQD (**F**). Snapshot structures of Aβ (**G**), Aβ +LPS (**H**), Aβ+CQD (**J**) and Aβ+CQD+LPS (**K**). Binding frequency of each Aβ residue with LPS (**I**) and CQD (**L**). In the snapshots, the peptides are shown as cartoons with distinct colors while LPS and CQD are illustrated as sticks in green and grey, respectively.

To elucidate the molecular mechanisms of the promotion effect of LPS and the inhibition effect of CQD on the aggregation processes of IAPP and Aβ, the binding probabilities of the peptides with LPS and CQD were calculated. The binding of LPS with IAPP and Aβ was dominated by the hydrophobic tail of the LPS, while the binding with the head of LPS was mainly contributed by electrostatic interactions (**Fig. 4A-C, G-I**). LPS displayed strong binding for the N-terminus of IAPP and weak binding for the C-terminus (**Fig. 4C**). Therefore, LPS recruited IAPPs via hydrophobic and electrostatic interactions with the N-termini, subsequently increasing the local IAPP concentration and enhancing inter-chain interactions between the amyloidogenic regions near the IAPP C-terminus to promote IAPP fibrillization. With the net charges of both Aβ and LPS being negative, the binding with Aβ was mainly driven by hydrophobic interaction with the LPS tail. LPS displayed strong binding preference towards both the central hydrophobic core (residues 17-21) and C-terminus but weak binding with the N-terminus of Aβ (**Fig. 4I**). By increasing the inter-chain contacts and β-sheet contents of these two binding regions in Aβ as well as facilitating inter-registered parallel alignments of the peptides (**Fig. 3D, G, H**), LPS promoted Aβ fibrillization.

CQDs exhibited strong binding with IAPP and Aβ in simulations. Specifically, all residues of IAPP except the N-terminal residues 1-10 had binding frequencies near 1.0 with the CQD, while the N-terminal residues 4-15 of Aβ were the preferred CQD-binding region (**Fig. 4E&F, J-L)**. After adsorbed onto the CQD surface, peptides preferred to bind with CQD instead of other peptides, resulting into the reduction of the inter-peptides contacts (**Fig. S4C&D, G&H**) and subsequent fibrillization inhibition. It is worth noting that the binding frequency of the Aβ amyloidogenic region (16-22) was relatively low due to the electrostatic repulsion between negatively charged CQDs and the flanking same-charged residues E22 and D23. As a result, further Aβ fibrillization was still possible, which explains the observation of small Aβ (proto)fibrils in the presence of CQDs in TEM imaging (**Fig. 2I**). On the other hand, while CQDs could form strong contacts with the peptides, the presence of LPS could compromise the interactions between the peptides and CQDs, thereby reducing the mitigation capacity of the nanoparticles against peptide fibrillization (**Fig. 4F&L**).

***In vivo* IAPP and Aβ amyloidosis acceleration with LPS and their inhibition with CQDs**

Zebrafish embryos were used as model systems to study the effect of LPS on the peptide aggregation and toxicity as well as their mitigation with CQDs. Zebrafish is a good model due to its high resistance to LPS toxicity, enabling the assessment of the LPS-induced IAPP and Aβ amyloidosis toxicity without the co-occurring toxicity of LPS.[80]

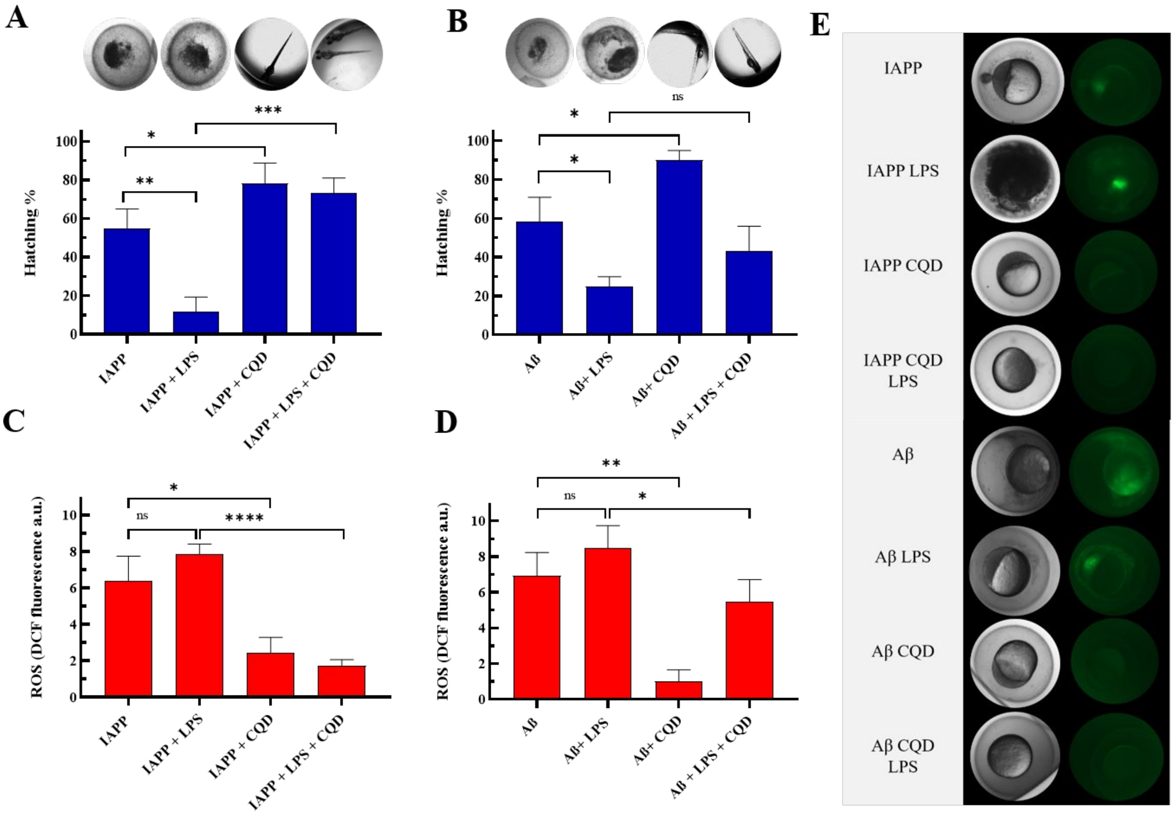

Figure 5. Development of zebrafish embryos in the presence of IAPP and Aβ, and modulated by LPS and CQDs. Zebrafish embryos (3 hpf) were microinjected with IAPP (10 μM) or Aβ (10 μM), with or without LPS (1 μM) and CQDs (0.5 μg/mL). Survival of the embryos was assessed by observing the hatching rate 3 days post injections. Resulting hatching rate after co-injecting LPS and CQDs with IAPP (**A**) and Aβ (**B**) and ROS response after IAPP (**C**) and Aβ injections (**D**). ThT fluorescence when co-injecting the peptides with LPS (**E**). Injecting CQDs with the peptides and LPS resulted in disappearance in ThT fluorescence (**E**), indicating absence of β-sheet rich fibrils. P <0.05 *; < 0.005 **; < 0.001***; < 0.0005****.

We decided to microinject IAPP and Aβ, with or without CQDs, as this approach required minimal sample volumes, facilitated the interactions of samples with embryonic cells, and allowed direct observation of toxicity. Direct co-incubation of the samples with embryos, in comparison, would require much greater sample consumptions, which could clog the chorionic pores and reduce the interactions of the samples with embryonic cells.[41] Microinjection of IAPP or Aβ to zebrafish embryos resulted in a near 50% reduction in larvae survival, compared to the untreated controls (**Fig. 5A&B, Fig. S8**). Co-injecting LPS at its non-lethal concentration (1 μM) with the peptides further reduced the hatching rate by 43% and 33% for IAPP and Aβ, leading to a total survival rate of 12% for IAPP and 25% for Aβ, respectively. This is in accordance with the ROS measurement, where a 33% and 25% increase in ROS production occurred for IAPP and Aβ when they were co-injected with LPS, validating the catalytic effect of the bacterial endotoxin on amyloidosis (**Fig. 5C&D, Fig. S8**).

CQDs have been shown in the literature as a biocompatible nanomaterial.[81] This was supported by our *in vivo* experiments, where injecting CQDs in zebrafish embryos did not interfere with the normal hatching rate or cause elevated ROS production (**Figs. S8&5**). Injecting CQDs with the peptides, in comparison, restored the embryo survival rate by 23% and 32% for IAPP and Aβ, respectively. In addition, the peptide toxicity was alleviated by CQDs in the presence of LPS, yielding a total survival rate of 73% for IAPP-LPS-CQD and 43% for Aβ-LPS-CQD (**Fig. 5A&B**). While CQDs displayed a greater mitigation potential against IAPP amyloidosis than Aβ, especially in the presence of LPS, CQDs were potent in ameliorating amyloidosis in both cases. This was also evident from the fluorescence images taken at 3 h post injection, where concentrated signals from the ThT-stained amyloids disappeared when the peptides were co-injected with CQDs (**Fig. 5E**). The decreased ROS production also indicated that CQDs were effective in mitigating the peptide toxicity (**Fig. 5C&D**).

Conclusion

Peptide amyloid aggregation is a hallmark of T2D and AD, whose pathologies also correlate with the dysbiosis of gut microbiota and elevated inflammation. T2D and AD subjects commonly show reduced diversity with the dominance of pro-inflammatory bacteria,[17] which constantly shed their outer cell wall components such as LPS into the surrounding environments. LPS can aggregate to resemble cell membranes, which are known to accelerate peptide fibrillization by acting as a nucleation substrate. In this study, we found that bacterial endotoxin LPS not only interacted with Aβ, as reported previously, but also with IAPP, an important finding that is pertinent to the origin of T2D but has been so far overlooked. Our DMD simulations also revealed that both IAPP and Aβ interacted with LPS, but via different binding patterns. Whereas LPS locally concentrated IAPP to facilitate the first steps in fibrillization, the endotoxin promoted in-register parallel β-sheet formation in Aβ, a necessary precursor towards the formation of amyloid fibrils. This accelerated peptide aggregation by LPS, however, was counteracted by CQDs *in vitro*, *in silico* and *in vivo*. CQDs specifically interacted and inhibited IAPP and Aβ, despite the presence of different glycoproteins, hatching enzymes and metabolites/cytokines in the chorionic fluid of zebrafish embryos.[82,83] This specificity can be attributed to the highly amphiphilic nature of CQDs and hence their propensity for the amyloid peptides via hydrophobic and H-bonding interactions. This study facilitated our understanding of the pathological connection between bacterial metabolites and amyloid diseases, and demonstrated the potential of CQDs as an anti-amyloidosis nanomedicine.

Electronic Supplementary Information (ESI): XPS spectra with curve fitting (Fig. S1), TEM of IAPP and Aβ interacting with LPS (Fig. S2), ThT fluorescence of CQDs, LPS and ThT dye (Fig. S3), aggregation dynamics of IAPP and Aβ, in the presence and absence of LPS and a

CQD, as revealed by DMD simulations (Fig. S4), secondary structures of IAPP and Aβ in the presence of LPS and CQDs, obtained by FTIR spectral deconvolution analyses and DMD simulations (Figs. S5&S6), solved Aβ fibril structures (Fig. S7), hatching rates and ROS levels of zebrafish exposed to control treatments (Fig. S8), and band assignments in FTIR spectroscopy (Table S1).

ACKNOWLEDGMENT

This work was supported by ARC Project No. CE140100036 (Davis), NSF CAREER CBET-1553945 (Ding) and NIH MIRA R35GM119691 (Ding). TEM imaging was performed at Bio21 Advanced Microscopy Facility, University of Melbourne. We thank Dr. Thomas Gengenbach, CSIRO for provision of the XPS data.

Conflicts of interest statement

There are no conflicts to declare.

Author contributions

PCK, KK and MM conceived the project. KK, PCK and HT wrote the manuscript. KK performed the ThT, TEM and FTIR assays and data analyses. IJ and SL performed the embryonic hatching and ROS assays. MP and AC synthesized and characterized the CQDs. HT and FD performed DMD simulations. All authors agreed on the presentation of the manuscript.

References

1. J. L. Leahy, *Arch. Med. Res.*, 2005, **36**, 197–209.
2. F. Zhang, M. Gannon, Y. Chen, S. Yan, S. Zhang, W. Feng, J. Tao, B. Sha, Z. Liu, T. Saito, T. Saido, C. D. Keene, K. Jiao, E. D. Roberson, H. Xu, and Q. Wang, *Sci. Transl. Med.*, 2020, **12**. eaay6931.
3. J. M. Long and D. M. Holtzman, *Cell*, 2019, **179**, 312–339.
4. S. Zraika, R. L. Hull, C. B. Verchere, A. Clark, K. J. Potter, P. E. Fraser, D. P. Raleigh, and S. E. Kahn, *Diabetologia*, 2010, **53**, 1046–1056.
5. P. C. Ke, M.-A. Sani, F. Ding, A. Kakinen, I. Javed, F. Separovic, T. P. Davis, and R. Mezzenga, *Chem. Soc. Rev.*, 2017, **46**, 6492–6531.
6. M. Nishi, T. Sanke, S. Nagamatsu, G. I. Bell, and D. F. Steiner, *J. Biol. Chem.*, 1990, **265**, 4173–4176.
7. P. Westermark, A. Andersson, and G. T. Westermark, *Physiol. Rev.*, 2011, **91**, 795–826.
8. H. Zheng, M. Jiang, M. E. Trumbauer, D. J. Sirinathsinghji, R. Hopkins, D. W. Smith, R. P. Heavens, G. R. Dawson, S. Boyce, M. W. Conner, K. A. Stevens, H. H. Slunt, S. S. Sisoda, H. Y. Chen, and L. H. Van der Ploeg, *Cell*, 1995, **81**, 525–531.
9. M. Hiltunen, T. van Groen, and J. Jolkkonen, *J. Alzheimers Dis.*, 2009, **18**, 401–412.
10. E. Stroo, M. Koopman, E. A. A. Nollen, and A. Mata-Cabana, *Front. Neurosci.*, 2017, **11**, 64.
11. J. W. Kelly, *Curr. Opin. Struct. Biol.*, 1998, **8**, 101–106.
12. S. I. A. Cohen, S. Linse, L. M. Luheshi, E. Hellstrand, D. A. White, L. Rajah, D. E. Otzen, M. Vendruscolo, C. M. Dobson, and T. P. J. Knowles, *Proc. Natl. Acad. Sci. USA*, 2013, **110**, 9758–9763.
13. T. R. Sampson, J. W. Debelius, T. Thron, S. Janssen, G. G. Shastri, Z. E. Ilhan, C. Challis, C. E. Schretter, S. Rocha, V. Gradinaru, M.-F. Chesselet, A. Keshavarzian, K. M. Shannon, R. Krajmalnik-Brown, P. Wittung-Stafshede, R. Knight, and S. K. Mazmanian, *Cell*, 2016, **167**, 1469–1480.e12.
14. S. F. Santos, H. L. de Oliveira, E. S. Yamada, B. C. Neves, and A. Pereira, *Front. Neurol.*, 2019, **10**, 574.
15. G. Sharon, T. R. Sampson, D. H. Geschwind, and S. K. Mazmanian, *Cell*, 2016, **167**, 915–932.
16. N. M. Vogt, R. L. Kerby, K. A. Dill-McFarland, S. J. Harding, A. P. Merluzzi, S. C. Johnson, C. M. Carlsson, S. Asthana, H. Zetterberg, K. Blennow, B. B. Bendlin, and F. E. Rey, *Sci. Rep.*, 2017, **7**, 13537.
17. A. Cattaneo, N. Cattane, S. Galluzzi, S. Provasi, N. Lopizzo, C. Festari, C. Ferrari, U. P. Guerra, B. Paghera, C. Muscio, A. Bianchetti, G. D. Volta, M. Turla, M. S. Cotelli, M. Gennuso, A. Prelle, O. Zanetti, G. Lussignoli, D. Mirabile, D. Bellandi, S. Gentile, G. Belotti, D. Villani, T. Harach, T. Bolmont, A. Padovani, M. Boccardi, G. B. Frisoni, and INDIA-FBP Group, *Neurobiol. Aging*, 2017, **49**, 60–68.
18. Z. Zhang, H. Tang, P. Chen, H. Xie, and Y. Tao, *Signal Transduct. Target. Ther.*, 2019, **4**, 41.
19. R. Nau and H. Eiffert, *Clin. Microbiol. Rev.*, 2002, **15**, 95–110.
20. S. Zhu, Y. Jiang, K. Xu, M. Cui, W. Ye, G. Zhao, L. Jin, and X. Chen, *J. Neuroinflamm.*, 2020, **17**, 25.
21. C. Galanos, O. Lüderitz, E. T. Rietschel, O. Westphal, H. Brade, L. Brade, M. Freudenberg, U. Schade, M. Imoto, and H. Yoshimura, *Eur. J. Biochem.*, 1985, **148**, 1–5.

22. C. Alexander and E. T. Rietschel, *J Endotoxin Res*, 2001, 7, 167–202.
23. X. Zhan, C. Cox, B. P. Ander, D. Liu, B. Stamova, L.-W. Jin, G. C. Jickling, and F. R. Sharp, *J. Alzheimers Dis.*, 2015, **46**, 507–523.
24. J. Zhou, W. Yu, M. Zhang, X. Tian, Y. Li, and Y. Lü, *Neurochem. Res.*, 2019, **44**, 1138–1151.
25. B. Hauss-Wegrzyniak, P. Dobrzanski, J. D. Stoehr, and G. L. Wenk, *Brain Res.*, 1998, **780**, 294–303.
26. C. Y. D. Lee and G. E. Landreth, *J. Neural Transm.*, 2010, **117**, 949–960.
27. X. Zhan, B. Stamova, L.-W. Jin, C. DeCarli, B. Phinney, and F. R. Sharp, *Neurology*, 2016, **87**, 2324–2332.
28. Y. Zhao, L. Cong, V. Jaber, and W. J. Lukiw, *Front. Immunol.*, 2017, **8**, 1064.
29. I. H. Philippens, P. R. Ormel, G. Baarends, M. Johansson, E. J. Remarque, and M. Doverskog, *J. Alzheimers Dis.*, 2017, **55**, 101–113.
30. P. C. Ke, E. H. Pilkington, Y. Sun, I. Javed, A. Kakinen, G. Peng, F. Ding, and T. P. Davis, *Adv. Mater.*, 2020, **32**, 1901690.
31. N. Gao, H. Sun, K. Dong, J. Ren, T. Duan, C. Xu, and X. Qu, *Nat. Commun.*, 2014, **5**, 3422.
32. I. Javed, G. Peng, Y. Xing, T. Yu, M. Zhao, A. Kakinen, A. Faridi, C. L. Parish, F. Ding, T. P. Davis, P. C. Ke, and S. Lin, *Nat. Commun.*, 2019, **10**, 3780.
33. I. Javed, J. He, A. Kakinen, A. Faridi, W. Yang, T. P. Davis, P. C. Ke, and P. Chen, *ACS Appl. Mater. Interfaces*, 2019, **11**, 10462–10471.
34. A. Faridi, Y. Sun, Y. Okazaki, G. Peng, J. Gao, A. Kakinen, P. Faridi, M. Zhao, I. Javed, A. W. Purcell, T. P. Davis, S. Lin, R. Oda, F. Ding, and P. C. Ke, *Small*, 2018, **14**, e1802825.
35. M. Wang, Y. Sun, X. Cao, G. Peng, I. Javed, A. Kakinen, T. P. Davis, S. Lin, J. Liu, F. Ding, and P. C. Ke, *Nanoscale*, 2018, **10**, 19995–20006.
36. E. N. Gurzov, B. Wang, E. H. Pilkington, P. Chen, A. Kakinen, W. J. Stanley, S. A. Litwak, E. G. Hanssen, T. P. Davis, F. Ding, and P. C. Ke, *Small*, 2016, **12**, 1615–1626.
37. Y. Zhou, P. Y. Liyanage, D. Devadoss, L. R. Rios Guevara, L. Cheng, R. M. Graham, H. S. Chand, A. O. Al-Youbi, A. S. Bashammakh, M. S. El-Shahawi, and R. M. Leblanc, *Nanoscale*, 2019, **11**, 22387–22397.
38. X. Xu, R. Ray, Y. Gu, H. J. Ploehn, L. Gearheart, K. Raker, and W. A. Scrivens, *J. Am. Chem. Soc.*, 2004, **126**, 12736–12737.
39. S. Li, L. Wang, C. C. Chusuei, V. M. Suarez, P. L. Blackwelder, M. Micic, J. Orbulescu, and R. M. Leblanc, *Chem. Mater.*, 2015, **27**, 1764–1771.
40. X. Han, Z. Jing, W. Wu, B. Zou, Z. Peng, P. Ren, A. Wikramanayake, Z. Lu, and R. M. Leblanc, *Nanoscale*, 2017, **9**, 12862–12866.
41. I. Javed, T. Yu, G. Peng, A. Sánchez-Ferrer, A. Faridi, A. Kakinen, M. Zhao, R. Mezzenga, T. P. Davis, S. Lin, and P. C. Ke, *Nano Lett.*, 2018, **18**, 5797–5804.
42. F. Ding, D. Tsao, H. Nie, and N. V. Dokholyan, *Structure*, 2008, **16**, 1010–1018.
43. M. P. Allen and D. J. Tildesley, *Computer simulation of liquids*, Oxford University Press, 2017, vol. 1.
44. S. J. Bunce, Y. Wang, K. L. Stewart, A. E. Ashcroft, S. E. Radford, C. K. Hall, and A. J. Wilson, *Sci. Adv.*, 2019, **5**, eaav8216.
45. K. I. Popov, K. A. Makepeace, E. V. Petrotchenko, N. V. Dokholyan, and C. H. Borchers, *Structure*, 2019, **27**, 1710–1715.

46. P. Sfriso, A. Emperador, L. Orellana, A. Hospital, J. L. Gelpí, and M. Orozco, *J. Chem. Theory Comput.*, 2012, **8**, 4707–4718.
47. F. Ding and N. V. Dokholyan, *PLoS Comput. Biol.*, 2006, **2**, e85.
48. S. Yin, F. Ding, and N. V. Dokholyan, *Nature Methods*, 2007, **4**, 466–467.
49. S. Yin, L. Biedermannova, J. Vondrasek, and N.V. Dokholyan, *J. Chem. Inf. Model.* 2008, **48**, 1656–1662.
50. E. Neria, S. Fischer, and M. Karplus, *J. Chem. Phys.*, 1996, **105**, 1902.
51. T. Lazaridis and M. Karplus, *Curr. Opin. Struct. Biol.*, 2000, **10**, 139–145.
52. F. Ding, J. M. Borreguero, S. V. Buldyrey, H. E. Stanley, and N. V. Dokholyan, *Proteins*, 2003, **53**, 220–228.
53. S. Kim, J. Chen, T. Cheng, A. Gindulyte, J. He, S. He, Q. Li, B. A. Shoemaker, P. A. Thiessen, B. Yu, L. Zaslavsky, J. Zhang, and E. E. Bolton, *Nucleic Acids Res.*, 2019, **47**, D1102–D1109.
54. M. D. Hanwell, D. E. Curtis, D. C. Lonie, T. Vandermeersch, E. Zurek, and G. R. Hutchison, *J. Cheminform.*, 2012, **4**, 17.
55. W. Kabsch and C. Sander, *Biopolymers*, 1983, **22**, 2577–2637.
56. G. Chen, S. Wu, L. Hui, Y. Zhao, J. Ye, Z. Tan, W. Zeng, Z. Tao, L. Yang, and Y. Zhu, *Sci. Rep.*, 2016, **6**, 19028.
57. M. R. Parsa and A. L. Chaffee, *Fuel*, 2019, **240**, 299–308.
58. X. Zhao, J. Zhang, L. Shi, M. Xian, C. Dong, and S. Shuang, *RSC Adv.*, 2017, **7**, 42159–42167.
59. A. Sadezky, H. Muckenhuber, H. Grothe, R. Niessner, and U. Pöschl, *Carbon*, 2005, **43**, 1731–1742.
60. L. Bokobza, J.-L. Bruneel, and M. Couzi, *C*, 2015, **1**, 77–94.
61. A. Dager, T. Uchida, T. Maekawa, and M. Tachibana, *Sci. Rep.*, 2019, **9**, 14004.
62. U. P. R. Agarwal, in *Proceedings of the 59th APPITA Annual Conference and Exhibition incorporating the 13th ISWFP*, 2005, pp. 1–8.
63. X. Liu, J. Pang, F. Xu, and X. Zhang, *Sci. Rep.*, 2016, **6**, 31100.
64. B. Mistry, H. K. Machhi, R. S. Vithalani, D. S. Patel, C. K. Modi, M. Prajapati, K. R. Surati, S. S. Soni, P. K. Jha, and S. R. Kane, *Sustainable Energy Fuels*, 2019, **3**, 3182–3190.
65. X. Miao, D. Qu, D. Yang, B. Nie, Y. Zhao, H. Fan, and Z. Sun, *Adv. Mater.*, 2018, **30**, 1704740.
66. Y.-E. Shin, Y. J. Sa, S. Park, J. Lee, K.-H. Shin, S. H. Joo, and H. Ko, *Nanoscale*, 2014, **6**, 9734–9741.
67. Z. Zhang, S. Lin, X. Li, H. Li, and W. Cui, *RSC Adv.*, 2017, **7**, 56335–56343.
68. A. Asti and L. Gioglio, *J. Alzheimers Dis.*, 2014, **39**, 169–179.
69. A. Sircana, L. Framarin, N. Leone, M. Berrutti, F. Castellino, R. Parente, F. De Michieli, E. Paschetta, and G. Musso, *Curr. Diab. Rep.*, 2018, **18**, 98.
70. M. I. Vaccaro, E. L. Calvo, A. M. Suburo, D. O. Sordelli, G. Lanosa, and J. L. Iovanna, *Dig. Dis. Sci.*, 2000, **45**, 915–926.
71. H. Sasaki and S. H. White, *Biophys. J.*, 2008, **95**, 986–993.
72. E. T. Rietschel, T. Kirikae, F. U. Schade, U. Mamat, G. Schmidt, H. Loppnow, A. J. Ulmer, U. Zähringer, U. Seydel, and F. Di Padova, *FASEB J.*, 1994, **8**, 217–225.
73. J. Seeliger, K. Weise, N. Opitz, and R. Winter, *J. Mol. Biol.*, 2012, **421**, 348–363.
74. M.-A. Sani, J. D. Gehman, and F. Separovic, *FEBS Lett.*, 2011, **585**, 749–754.

75. Z. Najarzadeh, J. N. Pedersen, G. Christiansen, S. A. Shojaosadati, J. S. Pedersen, and D. E. Otzen, *Biochim. Biophys. Acta Proteins Proteom.*, 2019, **1867**, 140263.
76. K. K. Andersen, C. L. Oliveira, K. L. Larsen, F. M. Poulsen, T. H. Callisen, P. Westh, J. S. Pedersen, and D. Otzen, *J. Mol. Biol.*, 2009, **391**, 207–226.
77. A. K. Buell, *Biochem. J.*, 2019, **476**, 2677–2703.
78. Y. Guan, Z. Du, N. Gao, Y. Cao, X. Wang, P. Scott, H. Song, J. Ren, and X. Qu, *Sci. Adv.*, 2018, **4**, eaao6718.
79. B. Srour, S. Bruechert, S. L. A. Andrade, and P. Hellwig, *Methods Mol. Biol.*, 2017, **1635**, 195–203.
80. I. Berczi, L. Bertók, and T. Bereznai, *Can. J. Microbiol.*, 1966, **12**, 1070–1071.
81. V. Mishra, A. Patil, S. Thakur, and P. Kesharwani, *Drug Discov. Today*, 2018, **23**, 1219–1232.
82. A. Okada, K. Sano, K. Nagata, S. Yasumasu, J. Ohtsuka, A. Yamamura, K. Kubota, I. Iuchi, and M. Tanokura, *J. Mol. Biol.*, 2010, **402**, 865–878.
83. T. Xia, Y. Zhao, T. Sager, S. George, S. Pokhrel, N. Li, D. Schoenfeld, H. Meng, S. Lin, X. Wang, M. Wang, Z. Ji, J. I. Zink, L. Mädler, V. Castranova, S. Lin, and A. E. Nel, *ACS Nano*, 2011, **5**, 1223–1235.

Table of Content Figure

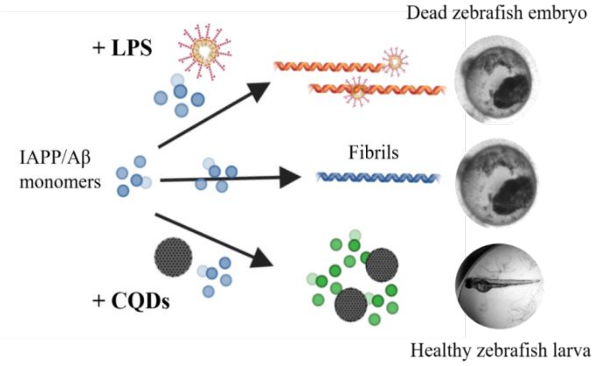

CQDs were potent in inhibiting IAPP and Aβ amyloidosis, allowing hatching of zebrafish embryos into healthy larvae.